Optics & Laser Technology 174 (2024) 110649

Contents lists available at ScienceDirect

Optics and Laser Technology

journal homepage: www.elsevier.com/locate/optlastec

Full length article

Tailoring the microstructure of Fe-2.9wt.%Si alloy in laser powder bed fusion using in-source beam shaping

Francesco Galbusera *, Leonardo Caprio, Barbara Previtali, Ali Gökhan Demir

Department of Mechanical Engineering, Politecnico di Milano, Via La Masa 1, I-20156 Milan, Italy

ARTICLE INFO

Keywords:
Beam shaping
Irradiance profile
Non-Gaussian beams
Ring beams
Laser powder bed fusion
Additive manufacturing
Soft magnets

ABSTRACT

Tuning the irradiance profile of the laser beam opens up new possibilities in terms of controlling the thermal field the material is subjected to during laser powder bed fusion (PBF-LB/M). This control can be exploited to manipulate the material's microstructure. In this work, a contemporary high power fibre laser with in-source beam shaping capability was used to test different irradiance profiles ranging from Gaussian to ring during the PBF-LB/M of Fe-2.9wt.%Si alloy. This soft magnetic alloy is used in electrical machines, and its magnetic properties are known to be correlated to the microstructure. Initially, the experimental work assessed the influence of peak and ring irradiance levels on densification and grain morphology. In a second experimental run, the influence of the beam profile on the conventionally employed energy density was verified. The results demonstrated that the use of combined Gaussian-ring profiles offers a method for manipulating grain size and shape from a columnar towards an equiaxed shape, without requiring a change in the scan strategy.

1. Introduction

Iron silicon alloys are well-known binary and soft magnetic materials used in the manufacturing of electromagnetic cores of stators, rotors, transformers, converters, and actuators. The combination of their excellent magnetic properties (such as the low power losses or the high saturation polarisation) and low price justifies their use for low switching frequency application (50–60 Hz) devices [1]. To match the demanding and growing performance requirements for small and lightweight next-generation electric motors, Additive Manufacturing (AM) technologies have recently attracted interest [2]. Indeed, AM could allow the construction of complex-shaped 3D iron cores [3], with engineered flux paths that overcome the conventional assembly limitations and integrated cooling channels [4]. At the same time, topological optimisation can be combined with new magnetic core concepts to reduce weight and power loss of moving parts and maximise the performance of electric machines [5]. Laser Powder Bed Fusion (PBF-LB/M) stands out as the most suitable technique for the production of complex geometries using this alloy. Many electrical silicon steel compositions with a Si-content (wt.%) ranging from 2.9 to 6.9 have been processed using PBF-LB/M so far. Overall, a mature processability of these alloys has been demonstrated, with high printed material density (>99.9 %) combined with high spatial accuracy [6], despite the crack susceptibility of the material [7]. Besides densification, functional magnetic properties have been of interest, such as permeability, coercivity and power losses [8]. A reduction of detrimental eddy currents was demonstrated by Yang et al. [9] and Tiismus et al. [10] with structural grading strategies and powder/air gaps, respectively, but also with complex mesh structures [11], or with higher Si-content while also increasing crack susceptibility [12]. Often heat treatments were needed to relieve stresses [13] and to homogenise the microstructure [14] to move from a highl y anisotropic columnar towards a more homogenous equiaxed microstructure. By applying the processing strategies developed, Tiismus et al. [10], Urbanek et al. [15], Garibaldi et al. [16] and Gargalis et al. [17] successfully built rotor prototypes for synchronous machines or switched reluctance motors. Functional transformer core was demonstrated by Tiismus et al. [18] and Plotkowski et al. [19]. Although these encouraging studies demonstrated the good level of maturity reached by the PBF-LB/M process, comprehensive and application-oriented research is still needed [20]. Indeed, the narrow process feasibility of iron silicon alloys, their inherent cracking susceptibility and the need of post heat treatments slow down the industrial application of PBF-LB/M for manufacturing magnetic cores [21].

The use of novel beam spatial profiles combined with Fe-Si alloys with less crack susceptibility can be a potential solution to enhancing

* Corresponding author.
E-mail addresses: francesco.galbusera@polimi.it (F. Galbusera), leonardo.caprio@polimi.it (L. Caprio), barbara.previtali@polimi.it (B. Previtali), aligokhan.demir@polimi.it (A.G. Demir).

https://doi.org/10.1016/j.optlastec.2024.110649
Received 7 July 2023; Received in revised form 16 November 2023; Accepted 26 January 2024
Available online 12 February 2024

Nomenclature

CE	Circle equivalent diameter (μm)
BS	Beam shape index (non-dimensional)
d_0	Beam waist diameter (μm)
I	Irradiance (MW/cm^2)
I_{pk}	Peak irradiance (MW/cm^2)
I_r	Ring irradiance (MW/cm^2)
I_0	Standard parametrised peak irradiance (MW/cm^2)
r	Radial coordinate (μm)
E	Volumetric energy density (J/mm^3)
P	Laser power (W)
v	Scan speed (mm/s)
z	Layer thickness (μm)
h_d	Hatch distance (μm)
d_{min}	Grain minor axis (μm)
d_{max}	Grain major axis (μm)
AR	Grain aspect ratio (non-dimensional)
ρ	Relative density (non-dimensional)
$A_{pore,tot}$	Total area of the pores (mm^2)
A_{tot}	Total area of the section (mm^2)
TI	Texture index (non-dimensional)

electrical performance via microstructural control. The use of contemporary fibre lasers with in-source beam shaping capabilities can provide the means for flexible manipulation of the microstructure when and where required. Recent works demonstrated the use of novel beam profiles to move towards ring shaped beam during the PBF-LB/M of AISI 316L [22] and its spatter characteristics [23], AlSi10Mg [24], AlSi7Mg0.6 [25], AlMg4.5Mn [26] and Scalmalloy [27]. Roehling et al. [28] and Shi et al. [29] demonstrated how to manipulate the grain morphology using elliptical beam profiles with AISI 316L. Cloots et al. [30] demonstrated that the use of a doughnut beam shape could reduce the hot cracking susceptibility of IN738LC. Processability improvements due to a reduced keyhole formation tendency was demonstrated with Bessel beams [31]. Significant process stability improvements for PBF-LB/M of a CoCrMo alloy were also observed by Zhirnov et al. [32] and Metel et al. [33] using top-hat or doughnut profiles. The influence of novel beam shapes on melt pool formation requires greater understanding. Commonly, the form of the melt tracks is studied using cross-sectional analysis, which provides insights into the cooling conditions. On the other hand, high speed imaging techniques based on external illumination can be an effective way of comparing the melt track shape and size in-situ [34]. The use of external illumination sources along with high-speed cameras allows for relatively easy implementation for viewing the melt pool on the surface [35], while the use of synchrotron imaging may make it possible to analyse melt pool penetration [36].

Overall, comprehensive works showed promising consequences with spatial beam shaping applied to material processing. In the best of perspectives, the irradiance profiles can be effectively used to manipulate the microstructure, which is of primary importance for tailoring the functional properties of as-built parts avoiding heat treatments of the entire workpiece [28]. Changing the irradiance profile dynamically and on-the-fly could make realisation of graded 3D parts with space-dependent functional properties possible. However, revelatory research is still needed to unleash the inherent potential of light source engineering in material processing. For this purpose, in-source dynamic laser beam shaping should be assessed in multiple layered parts for producing 3D objects.

Accordingly, this paper investigates how the microstructural properties of a common soft magnetic Fe-2.9wt.%Si alloy can be controlled by tuning the irradiance profile during PBF-LB/M. First, the available irradiance profiles, from Gaussian towards ring distributions, provided by a multi-core fibre laser source with in-source beam shaping capabilities, were characterised. Two shape-encoding parameters were introduced to describe the irradiance profile structure, namely peak and ring intensities. Then, to understand the effects of different irradiance profiles, relative density and microstructure properties in terms of grain size and crystallographic texture were analysed.

2. Materials and methods

2.1. PBF-LB/M and beam shaping system

The investigation was conducted with an industrial PBF-LB/M system with open architecture (3D-NT LLA150, Torino, Italy). The system is coupled with a novel double-core fibre laser source with in-source beam shaping capabilities (Corona nLIGHT AFX 1000, nLIGHT Inc, Vancouver, Washington, USA). The source features a maximum power of 600 W when using the central single mode core and up to 1.2 kW, when operating with both the double cores of the fibre. The laser is designed to emit radiation in the infrared spectrum at a wavelength of 1070 nm.

The double-core fibre laser source has seven programmable spatial beam profiles, each identified by the *BSi* index, where *i* ranges from 0 for the Gaussian shape to 6 for the doughnut shape. As declared by the producer [37], the distinction between each mode can be made based on the power distribution between the fibre core and the annular ring, which is used to switch the laser beam power between the indexes within a ms time-scale. Table 1 shows the nominal power ratio between the annular ring (doughnut, multi-mode) and the fibre core (Gaussian, single mode) for each *BS* declared by the producer. As can be seen, when rising power is deviated towards to the annular ring, the spatial mode shifts from a Gaussian-like shape (BS0, BS1), to a ring-like distribution (BS2, BS3, BS4) and eventually to a doughnut-like distribution (BS5, BS6).

A beam profiler (Gentec Beamage Series USB 3.0, Quebec City, Canada) was used to reconstruct the beam shapes at a fixed laser power of 200 W and in correspondence of the beam waist diameter. The laser emission power in the different emission modes was calibrated using a power meter (W-3000-D55-SHC, Laserpoint, Vimodrone, Italy). The measurements were carried out according to the ISO11146 and ISO11670 standards. Table 1 shows the beam waist diameters (d_0) measured at $1/e^2$ level while Fig. 1 shows the reconstructed irradiance profiles acquired at 200 W in terms of beam irradiance *I* (MW/cm^2) and radial coordinate *r* (μm).

When the laser power is deviated towards the outer ring of the fibre, the beam waist diameter enlarges, going from 49 μm for the Gaussian mode (BS0) to 144 μm for the doughnut distribution (BS6). Consistently, as observed from Fig. 1, the main central irradiance peak reduces from 20.4 MW/cm^2 for index BS0 to 15.5 MW/cm^2 for index BS1. For indexes BS2-6, two visible shoulders appear at the tail of the distribution as a result of rising power on the outer ring. However, for BS2-4 the main irradiance peak remains in the centre of the distribution, going from 11.3 MW/cm^2 for index BS2, to 8.3 MW/cm^2 for index BS3, and to 3.4 MW/cm^2 for index BS4. On the contrary, for BS5-6 the irradiance peak shifts to the tails of the distribution. The maximum irradiance peak for index BS5 and BS6 is 1.6 MW/cm^2 and 1.8 MW/cm^2, respectively.

Table 1 also shows the closest *TEM* categorisation assignable to each spatial mode [38]. According to the Laguerre-Gaussian distribution, the TEM_{pl} of a distribution depends on the *p* and *l* numbers, which are the number of radial and angular zero fields, respectively. Nonetheless, the *TEM* definitions provided in Table 1 give only close representations of the beam shapes since the profiles might be different from the analytical form of Laguerre-Gaussian modes. Thus, indexes BS0-1 can be addressed as TEM_{00} being close to a Gaussian profile. Instead, indexes BS2-4 resemble TEM_{10}, featuring a central irradiance peak surrounded by a ring. Index BS5 can be addressed as the superposition of TEM_{00} and TEM_{01^*} since the shape is similar to a flat top distribution, thus the superposition of a Gaussian and a doughnut profile. Finally, index BS6 can

Table 1
Power ratio between ring and core of the fibre, closest TEM representation and waist diameter d_0 for each beam shape index BS.

Beam shape (BS)	BS0	BS1	BS2	BS3	BS4	BS5	BS6
Power ratio (ring/core)	0/100	30/70	40/60	50/50	60/40	80/20	90/10
Closest Laguerre-Gaussian TEM	TEM_{00}	TEM_{00}	TEM_{10}	TEM_{10}	TEM_{10}	$TEM_{00} + TEM_{01^*}$	TEM_{01^*}
Beam diameter, d_0 (μm)	49	50	52	112	128	144	144

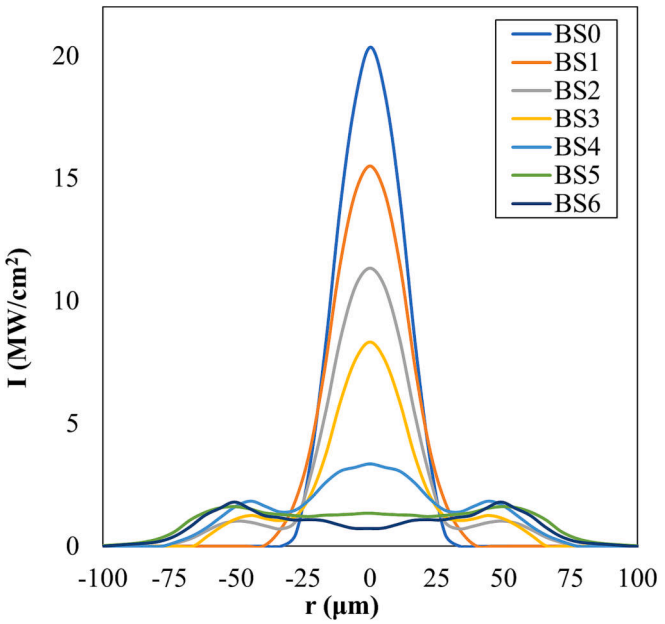

Fig. 1. Beam irradiance I as a function of the radial coordinate r for an emission power P = 200 W.

be represented by a TEM_{01^*} close to a pure doughnut profile.

2.2. Material

In this investigation a low-Si alloyed steel was processed. The feedstock was produced through powder atomisation (m4p material solutions GmbH, Feistritz, Austria). The declared nominal composition (wt.%) of the powder was 2.9 % Si and Fe (balance). The chemical composition was assessed by multiple measurements via electron diffraction spectroscopy on different areas of 1 mm^2. The measured chemical composition (wt.%) was 2.83 ± 0.21 Si and 97.17 ± 0.21 Fe confirming the declared composition. As shown in Fig. 2a, the powder exhibited a spherical shape, with a declared granulometry of between 20 μm and 53 μm. Fig. 2b shows the estimated Circle Equivalent diameter (*CE*) of a powder batch analysed using static automated imaging (Morphologi 4, Malvern Panalytical Ltd, Malvern, UK). The graph confirms that almost 91 % of the detected particles had an equivalent diameter within the declared range with the remaining particles distributed over 10 μm < *CE* < 20 μm or 53 μm < *CE* < 88 μm. AISI316L stainless-steel baseplates were used as substrates.

2.3. Experimental plan

In order to assess the change of the material's microstructure from a columnar to a more equiaxed structure, the experimental work was carried out in two steps. The aim of the combined study was to confirm that the irradiance parameters should be tuned using conventional process parameters to control the microstructure of Fe-2.9wt.%Si in a reproducible manner. In both the stages, the laser source was operated with a continuous wave emission mode. For any tested beam profile index, the focal point of the laser beam was set on the powder bed. No baseplate preheating was applied. Prismatic samples with dimensions of 5 × 5 × 10 mm^3 were built directly on the baseplates without support structures. Therefore, the specimens were removed from the substrates with a linear saw without any deformation. All the samples were produced in an Ar-based inert atmosphere, with the PBF-LB/M system limiting the oxygen content down to 3000 ppm with periodic purging and filling cycles.

2.3.1. Effect of irradiance

In the first step, two shape-encoding parameters of the beam profile, namely peak and ring intensities, were varied along with scan speed, and their effect on density and microstructure properties was assessed. Peak and ring intensities can be defined as the local intensity peaks that characterise each beam profile in the origin and surrounded ring, respectively. Fig. 3a graphically represents the definition of peak (I_{pk}) and ring (I_r) intensities. The former refers to the maximum intensity reached in the core of the distribution, while the latter refers to the peak on the outer ring whenever power is redistributed on the outer core of the fibre ($BS_{i>1}$).

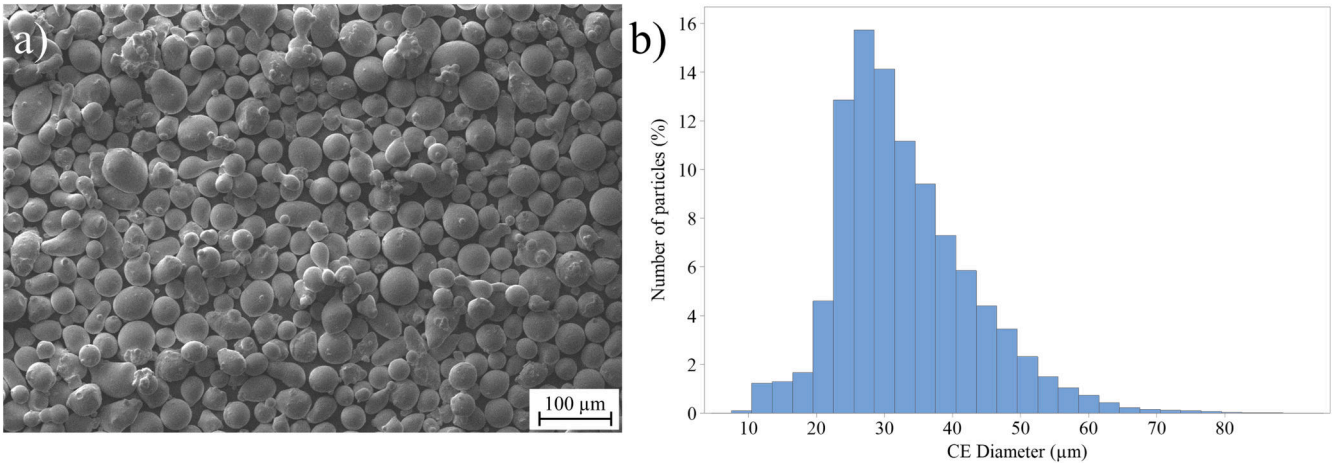

Fig. 2. a) SEM image and b) size distributions of the Fe-2.9 wt%Si powder feedstock.

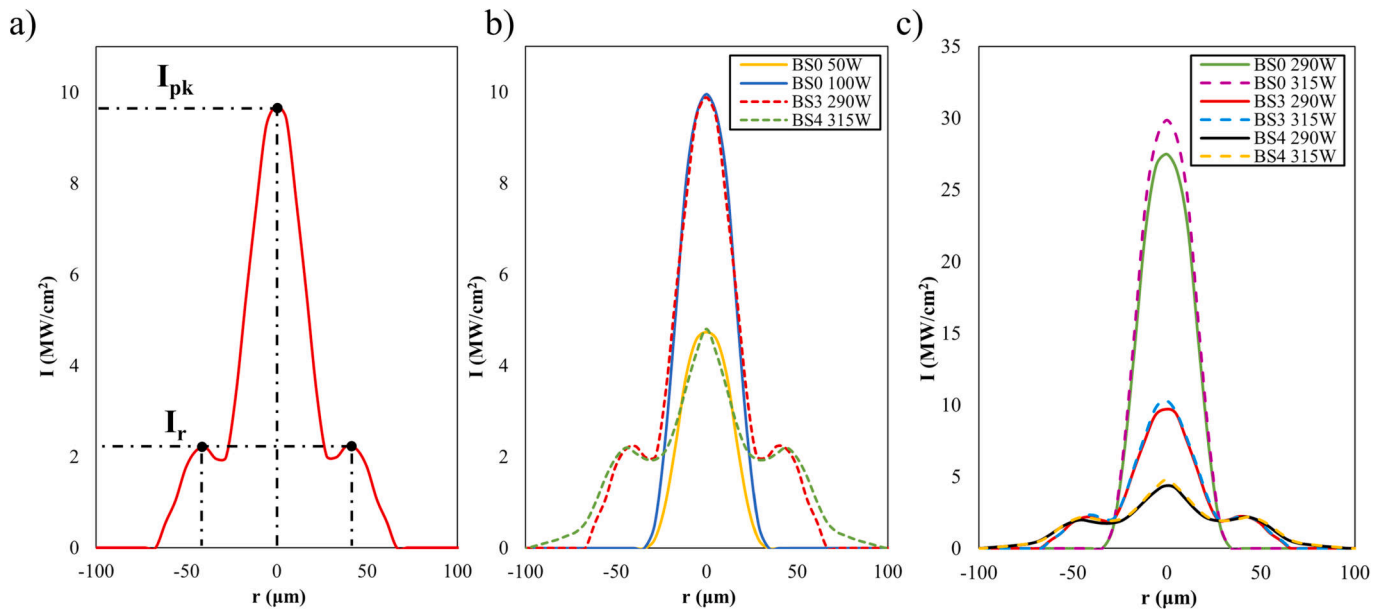

Fig. 3. a) Definition of peak (I_{pk}) and ring intensities (I_r); Measured irradiance profiles displayed as a function of the radial coordinate r for b) the first experimental step (effect of irradiance) and c) the second experimental step (effect of energy density, note that the irradiance axis range is different).

Two levels of I_{pk} were explored because it is believed that peak intensity controls the penetration depth, as observed in laser welding [39] and in a recent study with PBF-LB/M [25]. Moreover, two levels of I_r were investigated because, as demonstrated by a recent literature study, ring intensity can control the microstructure properties of as-built parts [27]. Beyond the irradiance parameters, a wide range of scan speeds (100 – 1300 mm/s) was explored to determine the conditions leading to high densification. Hatch distance and layer thickness were kept fixed at 70 and 30 μm, respectively. Owing to the exploratory nature of the experimental design, the conditions were not replicated. Table 2 shows the fixed and varied parameters used throughout this investigation.

The tested irradiance levels (I_{pk} and I_r) followed the parametrised scheme shown in Table 3. In order to achieve the same irradiance levels, the beam index was selected from those available and the power of the beam was adapted. A standard peak intensity I_0 was set using a Gaussian distribution (BS0) with a fixed power of 100 W. Therefore, to isolate the effect of the peak intensity, the same beam profile was run with half the power, namely 50 W, to guarantee testing of the other peak intensity condition, namely $I_0/2$. The ring intensity of the two Gaussian conditions is null because power is redistributed according to a Gaussian function within the central core of the fibre. To isolate the effect of the ring intensity, a defined I_r level of $0.2I_0$ was set. Consistently, the average power of two beam indexes, namely BS3 and BS4, was empirically tuned to match the peak intensities of I_0 and $I_0/2$ while providing an I_r of $0.2I_0$.

The reconstructed irradiance profiles of the conditions tested are shown in Fig. 3b in terms of irradiance I (MW/cm^2) and radial coordinate r (μm). BS0 and BS3 run at 100 and 290 W respectively achieve a peak intensity of 10.6 MW/cm^2 while BS0 and BS4 run at 50 and 315 W respectively achieve a peak intensity of 5.3 MW/cm^2. Meanwhile, only BS3 and BS4 achieve a ring intensity of 2.1 MW/cm^2.

Table 2
Fixed and varied process parameters used in the first experimental stage.

Fixed parameters	
Hatch distance, h_d, (μm)	70
Layer thickness, z, (μm)	30
Hatching rotation, (°)	67
Hatching strategy	Bidirectional
Inert gas type	Argon
Baseplate	AISI316L
Varied parameters	
Peak intensity, I_{pk} (MW/cm^2)	5.3, 10.6
Ring intensity, I_r (MW/cm^2)	0, 2.1
Scan speed, v (mm/s)	100, 250, 400, 550, 700, 850, 1000, 1150, 1300

Table 3
Beam shape index, parametrised irradiance intensity in terms of peak (I_{pk}) irradiance and ring (I_r) iradiance and the resulting power levels of the tested experimental conditions.

***BS* (–)**	***I_{pk}* (MW/cm^2)**	***I_r* (MW/cm^2)**	***P* (W)**
BS0	$I_0 = 10.6$	0 (Not added)	100
BS0	$0.5I_0 = 5.3$	0 (Not added)	50
BS3	$I_0 = 10.6$	$0.2I_0 = 2.1$	290
BS4	$0.5I_0 = 5.3$	$0.2I_0 = 2.1$	315

Adjusting the power level to parametrize the irradiance complicates the determination of appropriate scan speed levels to fabricate highly dense samples. This is one of the reasons why a broad range of scan speeds was explored in the experimental design. This design choice allowed to test a wide volumetric energy density (E) window between 18 J/mm^3 and 1500 J/mm^3, where the energy density E, commonly employed in PBF-LB/M to define the nominal energy released to the material, is defined as:

$$E = \frac{P}{v \cdot z \cdot h_d} \quad (1)$$

The experiments were carried out using a scan strategy that is commonly employed in industrial practice consisting of a bidirectional scan path rotated by 67° between each layer. Hence, the intended microstructural manipulation excluded the use of different scan strategies.

2.3.2. *Effect of energy density*

In the second step, to decouple the effect of the spatial beam profile from the volumetric energy density, the laser power, beam profile index and scan speed were varied consistently with the first study.

In this validation plan, the beam profiles of the highest power levels in the previous plan (BS3 and BS4 in Table 3) were compared to the Gaussian profile of the same power level. The reconstructed irradiance profiles of the tested conditions are shown in Fig. 3c in terms of

irradiance I (MW/cm^2) and radial coordinate r (μm). The Gaussian conditions (BS0) tested at 290 W and 315 W achieve peak intensities above 27 MW/cm^2, which is more than double the conditions with BS3 and fivefold the conditions with BS4. The ring intensities of the BS3-4 profiles do not change significantly, attaining around 2.1 MW/cm^2. In order to have results that are comparable with the previous experimental campaign, a restrained scan speed window of 100 – 250 mm/s, that led to adequate densification, was explored. All the other process parameters were kept fixed according to the previous experimental plan, as shown in Table 4.

2.4. Metallographic analysis

As-built samples were prepared for metallographic analysis following standard grinding and polishing procedures. Optical microscopy was used to acquire the polished cross sections orthogonal to the build direction (Mitutoyo, QV ELF202, Kanagawa, Japan). To measure relative density (ρ) as a quantitative measurement of porosity distribution, a conventional approach based on a digital image processing procedure was followed (ImageJ, U.S. National Institutes of Health, Bethesda, Maryland, USA) [40]. By applying a proper filtering procedure, the polished cross sections were converted into a black and white scale to distinguish bulky regions (white) from pores (black), and then the calculation of ρ becomes:

$$\rho\,(\%) = \left(1 - \frac{A_{pore,tot}}{A_{tot}}\right) * 100\% \tag{2}$$

where $A_{pore,tot}$ is the total area of the pores and A_{tot}, is the total area of the section (bulk and pores).

The microstructure was revealed after proper polishing using diamond abrasive pads (6 μm, 3 μm, 1 μm and SiC) and chemical etching with a Nital solution (2 % HNO_3 in ethanol) as suggested in literature [41].

In addition, grain size measurements were acquired from the metallographic optical images. For each tested condition shown in Table 2 and Table 4, the grain boundaries of a selected batch of grains were first reconstructed. An example of grain boundary reconstruction from optical microscopy images is presented in Fig. 4. Owing to the columnar nature of the grains encountered during the analysis, two spatial measurements of grain size were collected: the minor axis (d_{min}) and the major axis (d_{max}). Thus, the grain aspect ratio (AR) was calculated to get simple and representative insights into grain morphology using the following formula:

$$AR = \frac{d_{max}}{d_{min}} \tag{3}$$

According to this definition, grains featured by $AR < 2$ are considered equiaxed while the others are columnar [42]. An example of grain minor and major axis is shown in Fig. 4.

Detailed metallurgical analysis was conducted on the samples that exhibited the most significant microstructural changes with adequate densification ($v = 100$ mm/s, $I_{pk} = 5.3 – 10.6$ MW/cm^2, $I_r = 0 – 2.1$ MW/cm^2). Crystallographic texture and grain structure were investigated by means of Electron Back Scattered Diffraction (EBSD, Oxford Instruments C Nano) on a dedicated scanning electron microscope (Sigma 500 Zeiss FESEM, Oberkochen, Germany). Samples for EBSD analysis were mechanically grounded up to SiC papers, finely polished with 0.04 μm colloidal silica and kept under vibratory polishing (QPOL VIBRO, QATM, Mammelzen, Germany) using the same abrasive solution for 30 min to prepare the specimens' surfaces without any deformation. The data acquired was analysed using dedicated software (AZtec, Oxford Instruments NanoAnalysis, Abingdon, UK) and the Matlab toolbox MTEX. A step size of 1 μm, field width and height of 1.3 mm were used. Grains were defined as having a misorientation angle larger than 5°, following the suggestion by Garibaldi et al. in their study on Fe-6.9wt.% Si alloy [43]. Hence, grain boundary density was estimated by dividing the sum of grain boundary length for the acquisition field area. Texture index was also calculated as a measurement of the texture degree with the aid of MTEX and according to the following formula:

$$TI = \int f(g)^2 dg \tag{4}$$

where f represents the orientation distribution function and g the generic orientation.

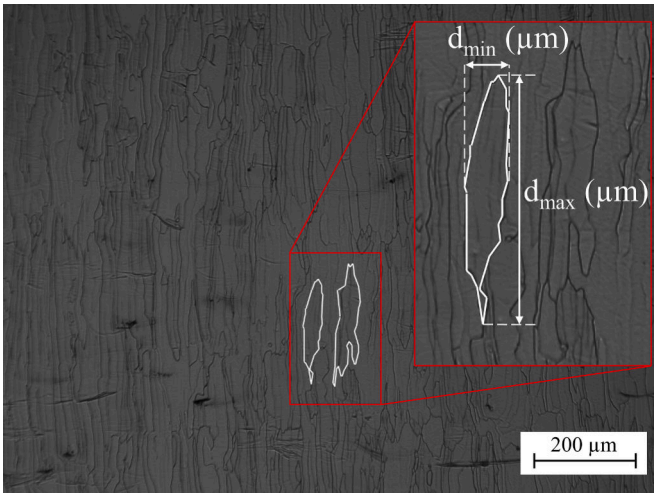

Fig. 4. Example of grain boundaries reconstruction from optical microscopy images with detail of the measured grain minor axis, d_{min}, and major axis, d_{max}.

Table 4
Fixed and varied process parameters used in the second experimental stage.

Fixed parameters	
Hatch distance, h_d, (μm)	70
Layer thickness, z, (μm)	30
Hatching rotation, (°)	67
Hatching strategy	Bidirectional
Inert gas type	Argon
Baseplate	AISI316L
Varied parameters	
Beam shape, *BS* (–)	BS0, BS3, BS4
Power, *P* (W)	290, 315
Scan speed, *v* (mm/s)	100, 250

2.5. High speed imaging

The melt pool size is hard to define over the metallographic cross-sections of PBF-LB/M processed Fe-Si alloys. Therefore, to visualize the in-situ melt pool form and size high speed imaging was used. Single layer bead on track analyses were carried out using the parameter sets for the conditions chosen for EBSD analysis. The tracks were monitored using a high-speed camera (Fastcam Mini AX200, Photron, Tokyo, Japan) to qualitatively investigate the melt pool dimensions. The camera featured a 1 mega pixel CMOS sensor and allowed acquisition of a region with dimensions of 1024 × 176 pixels at a spatial resolution of 4.6 μm/pixel. A secondary illumination light (Cavilux HF, Cavitar, Tampere, Finland), consisting of a pulsed laser source emitting light at 640 nm, was operated off-axis to ensure the proper quality of the frames acquired. Accordingly, the exposure time of the camera and the illumination pulse were tuned to guarantee the correct exposure, with an acquisition frequency of 25 kHz. Fig. 5 shows an overview of the monitoring setup integrated with the PBF-LB/M system. To observe the melt pool shape in real time while guaranteeing high spatial resolution, the camera was installed across the build chamber, thus impeding

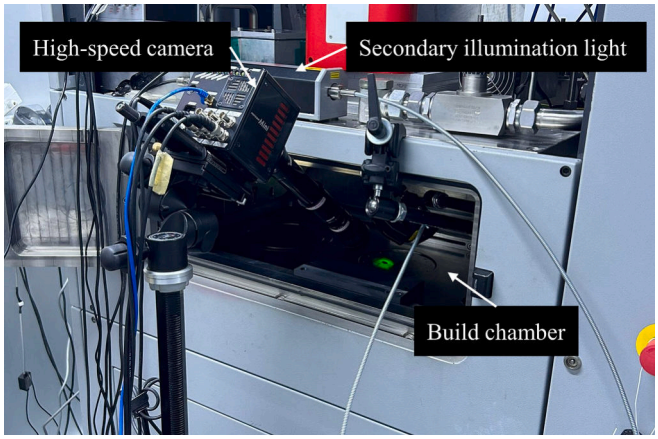

Fig. 5. Overview of the monitoring setup used for observing the melt pool shapes in real time. The setup is based on the synchronisation of the high-speed camera and secondary illumination light arranged in an off-axis architecture in relation to the incoming fibre laser source of the PBF-LB/M system.

working in an inert atmosphere. Despite operating the PBF-LB/M system with the open chamber, a localised shielding of argon was conveyed towards the single-track depositions.

3. Results

3.1. Influence of peak and ring irradiance

3.1.1. Densification

Fig. 6a presents relative density data as a function of process parameters. Data obtained with a Gaussian profile (left panel, $I_r = 0$ MW/cm^2) shows a decreasing trend as the scan speed increases. On the other hand, data on the ring beam conditions (right panel, $I_r = 2.1$ MW/cm^2) exhibit a constant trend with $\rho > 99.9$ %. It is evident that the application of additional ring intensity has resulted in an improvement in densification, achieving 99.9 % regardless of the peak intensity and scan speed used. This effect is more pronounced when $I_{pk} = I_0/2 = 5.3$ MW/cm^2 was used (blue connected line).

Fig. 6b shows the same ρ data in terms of energy density (E) and peak and ring irradiance intensities (I_{pk}, I_r). The red shaded area represented in the left panel ($I_r = 0$ MW/cm^2) refers to an insufficient relative density region with $\rho < 99$ %. Indicatively, the region is delimited by $E < 100$ J/mm^3 and $I_{pk} < 11$ MW/cm^2. The graph provides processability maps in terms of the total amount of energy input and the peak irradiance, for the two ring intensities tested. When a ring intensity is applied, ρ data does not define a non-acceptable processing zone. The overall analysis suggests that the densification is independent of the irradiance profile and depends overall on the energy density.

Fig. 7 shows the cross sections obtained for all the tested irradiance conditions in terms of peak (I_{pk}) and ring (I_r) intensities for two representative scan speed levels, 100 mm/s and 250 mm/s, where $\rho > 96$ %. For scan speeds greater than 250 mm/s, the densification of the samples tested at $I_{pk} = I_0/2$ and $I_r = 0$ decreases significantly below 90 % due to insufficient energy density ($E < 60$ J/mm^3). As a result, these speeds have been omitted from the comparison. Overall, the comparison shows that the use of the ring intensity has led to an improvement in sample densification. At $I_{pk} = I_0$ and $v = 100$ mm/s, the density ρ remained higher than 99.9 %. Similarly, for $v = 250$ mm/s, the additional power on the ring resulted in an increase in the density ρ from 99.1 to 99.9 %. This trend also holds true for the conditions obtained at $I_{pk} = I_0/2$ and $v = 250$ mm/s, where ρ increased from approximately 96.9 % to 99.9 %. On the contrary, for the conditions obtained at $I_{pk} = I_0/2$ and $v = 100$ mm/s, there was no significant increase in density (around 99.6 %). However, the porosity morphology changed between the two conditions: without I_r, the pores were mostly irregular and elongated in shape, while with $I_r = 0.2I_0$, the pores were mostly circular. It is important to note that the two conditions correspond to two different energetic input conditions, approximately 238 J/mm^3 for the former and 1500 J/mm^3 for the latter. The discrepancy in the energy densities can be readily explained by the varying average power content associated with the two beam shape indexes, as shown in Table 3. This difference in the energy density may account for the variation in porosity morphology observed. At high energy density levels, porosity could be attributed to keyhole porosity. Conversely, at lower energy density, the lack of a fusion mechanism may drive the formation of porosity.

3.1.2. Microstructure

Fig. 8 shows the microstructure for the same conditions as those shown in Fig. 7, which corresponds to all the irradiance levels tested at the speed levels of 100 and 250 mm/s. When the speed exceeds 250 mm/s, the primary microstructure consists of columnar and elongated grains along the build direction (BD). This direction coincides with the main heat flow direction, resulting in epitaxial growth during the entire

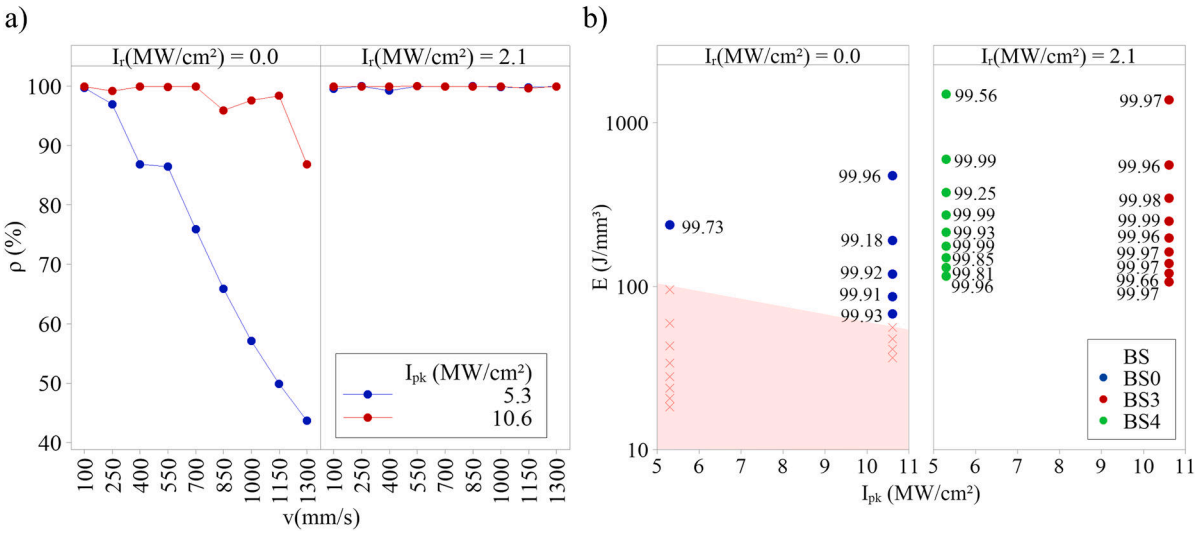

Fig. 6. a) Density (ρ) as a function of process parameters. b) Volumetric energy density (E) vs peak (I_{pk}) and ring (I_r) intensities for each experimental condition. Data labels denote the corresponding density. Red cross symbols in the shaded area refer to $\rho < 99$ % data with BS0. (For interpretation of the references to colour in this figure legend, the reader is referred to the web version of this article.)

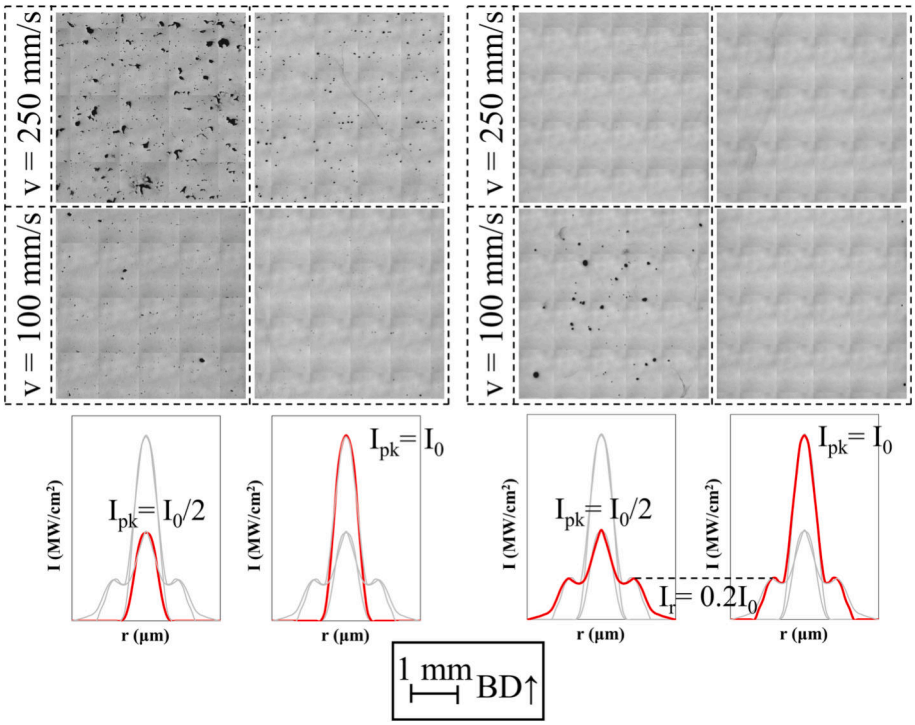

Fig. 7. Metallographic cross section comparison of the tested irradiance levels (I_{pk}, I_r) at the scan speed levels of 100 and 250 mm/s (BD: Build Direction).

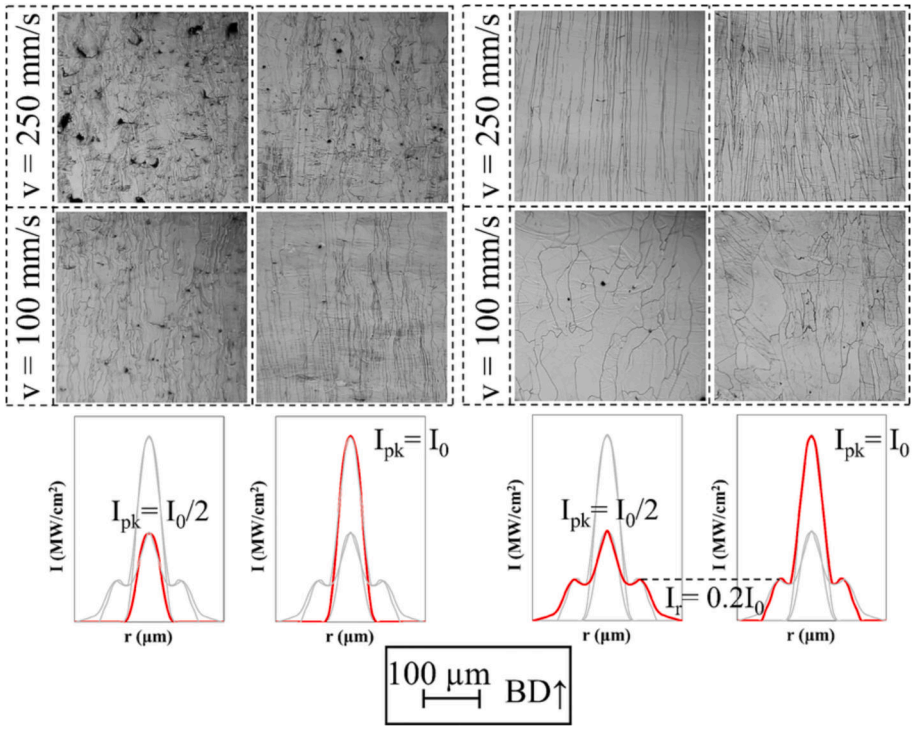

Fig. 8. Microstructure comparison of the irradiance levels (I_{pk}, I_r) tested at the scan speed levels of 100 and 250 mm/s (BD: Build Direction).

deposition process. According to Garibaldi et al. [43], this growth mechanism is attributed to a selection process in which grains that align with the solidification direction have a competitive advantage over grains with less favourable orientations, resulting in their superior growth. However, at a speed of 100 mm/s, the use of I_r led to the formation of larger and coarser grains. Although these grains still exhibited elongation along the build direction, they were not arranged in a columnar fashion, as occurred at the same scan speed levels without the application of I_r (Gaussian conditions). This distinct morphology is similar the microstructure observed after high-temperature (>1000°) annealing of as-built parts [13].

3.1.3. Grain size

Fig. 9a shows plotting of the main effects of grain aspect ratio (*AR*)

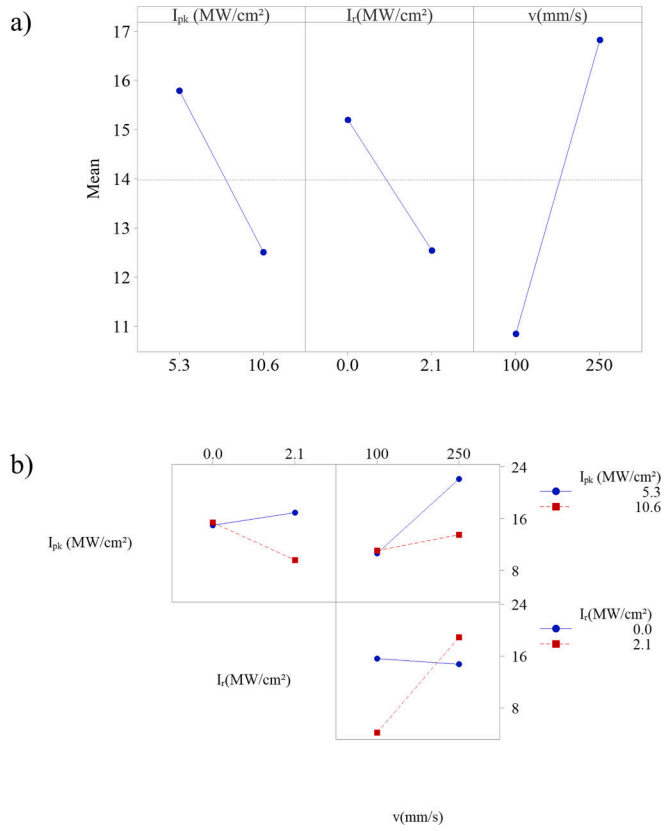

Fig. 9. a) Main and b) interaction plots of grain aspect ratio (*AR*).

data as a function of the experimental conditions. Within the tested experimental region, the scan speed had the strongest effect on *AR* followed by the peak and ring intensities. The interaction plot is presented in Fig. 9b. In each box, data is displayed as a function of the two parameters together, helping to identify potential interactions between two factors. When parallel lines are observed, it suggests the absence of interaction between the two factors being analysed. On the other hand, if the lines cross each other, it indicates the presence of an interaction. In this case, all the 2nd order interactions seem to be influential.

The main effects and interactions of all factors were assessed by an analysis of variance (ANOVA) and the results are shown in Table 5. The model comprises I_{pk}, I_r and v and their interactions up to the 3rd order. The model has an R^2_{adj} value of 78.24 %. Since all the statistical hypotheses are verified, it becomes evident that additional interpretations regarding the significance of the parameter are possible.

Except for I_{pk} and the interaction I_{pk}*I_r, whose p-value is > 0.05, all the other main factors and their interactions are significant as expected. Among others, the scan speed and its interaction with I_r have the largest influence given its highest F-value. Due to the incorporation of multiple high-order interactions, the model's complexity renders the development of a simple and intuitive formulation for *AR* unfeasible. Nevertheless, statistical data demonstrates that the use of the ring intensity is required to modify the microstructure from a columnar structure towards a lower *AR*. On the other hand, an increase in the ring intensity corresponds to an increase in the power level. Hence, the second experimental campaign is required to assess the grain morphology at the same power levels, and therefore the same energy density levels.

3.2. Verification at equivalent energy density

3.2.1. Densification

Fig. 10 shows the cross section obtained for all the power and scan speed levels tested and for each beam shape. The conditions obtained with a Gaussian profile (index BS0) at both scan speed and power levels are fully dense ($\rho > 99.8$ %). Lack of fusion porosity is not observed as per the high energy density levels involved. The conditions obtained with index BS3 are highly dense ($\rho > 99.6$ %) irrespective of the scan speed and power levels. Also, the conditions obtained with index BS4 are highly dense ($\rho > 99.4$ %), except for that obtained at $P = 315$ W and $v = 100$ mm/s which shows circular pores uniformly distributed over the cross section indicating an onset of a possible keyholing phenomenon. An aspect worth noting is that the conditions obtained with BS3 – $P = 290$ W and BS4 – $P = 315$ W were already tested in the first experimental phase based on irradiance parametrisation, where keyholing was observed as being likely associated to the high energy input provided ($E = 1500$ J/mm^3). The reduction of the energy density down to $E = 1381$ J/mm^3 induced by the reduced power content made it possible to significantly mitigate the porosity level.

Relative density data is provided as a function of the process parameters in Fig. 11a. Overall, adequate density higher than 99 % is maintained. Only the aforementioned condition with parameters BS4 – $P = 315$ W – $v = 100$ mm/s shows the lowest relative density. Fig. 11b reproduces the same ρ data in terms of energy density (E) and peak irradiance intensities (I_{pk}). All the conditions tested in terms of power, speed, and beam shape profile do not make it possible to identify not-acceptable regions ($\rho > 99$ %). It is worth noting that the conditions processed with a Gaussian profile enlarge the feasibility window going from $I_{pk} = 10.6$ MW/cm^2 (I_0) to over 30 MW/cm^2.

3.2.2. Microstructure

Fig. 12 shows the microstructure for the same conditions as those presented in Fig. 10. At $v = 250$ mm/s the microstructure consists of columnar grains that are elongated along the build direction, regardless

Table 5
Analysis of variance in the grain aspect ratio (*AR*) and model summary. The p-values of the statistically significant parameters are shown in bold.

Source	DF	Adj SS	Adj MS	F-Value	P-Value
I_{pk} (MW/cm^2)	1	0.1027	0.1027	1.04	0.312
I_r (MW/cm^2)	1	4.6995	4.6995	47.69	**0.000**
v (mm/s)	1	8.8431	8.8431	89.73	**0.000**
I_{pk} (MW/cm^2) * I_r (MW/cm^2)	1	0.1940	0.1940	1.97	0.166
I_{pk} (MW/cm^2) * v (mm/s)	1	2.6283	2.6283	26.67	**0.000**
I_r (MW/cm^2) * v (mm/s)	1	10.0874	10.0874	102.36	**0.000**
I_{pk} (MW/cm^2) * I_r (MW/cm^2) * v (mm/s)	1	1.8652	1.8652	18.93	**0.000**
Error	57	5.6174	0.0986		
Total	64	28.9910			

Model Summary

S	R-sq	R-sq(adj)	R-sq(pred)
0.313929	80.62 %	78.24 %	75.23 %

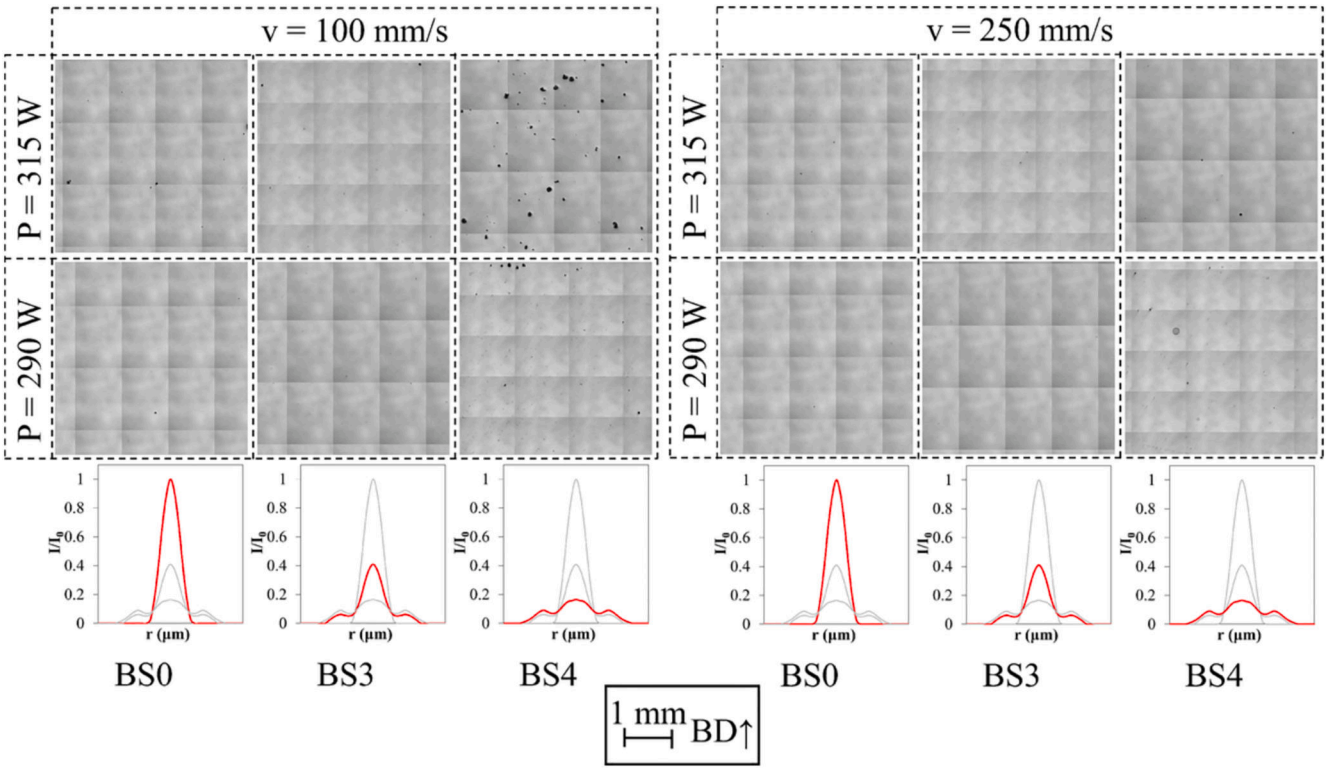

Fig. 10. Metallographic cross section comparison of the validation experiment in terms of *P*, *v* and beam shape *BS* (BD: Build Direction).

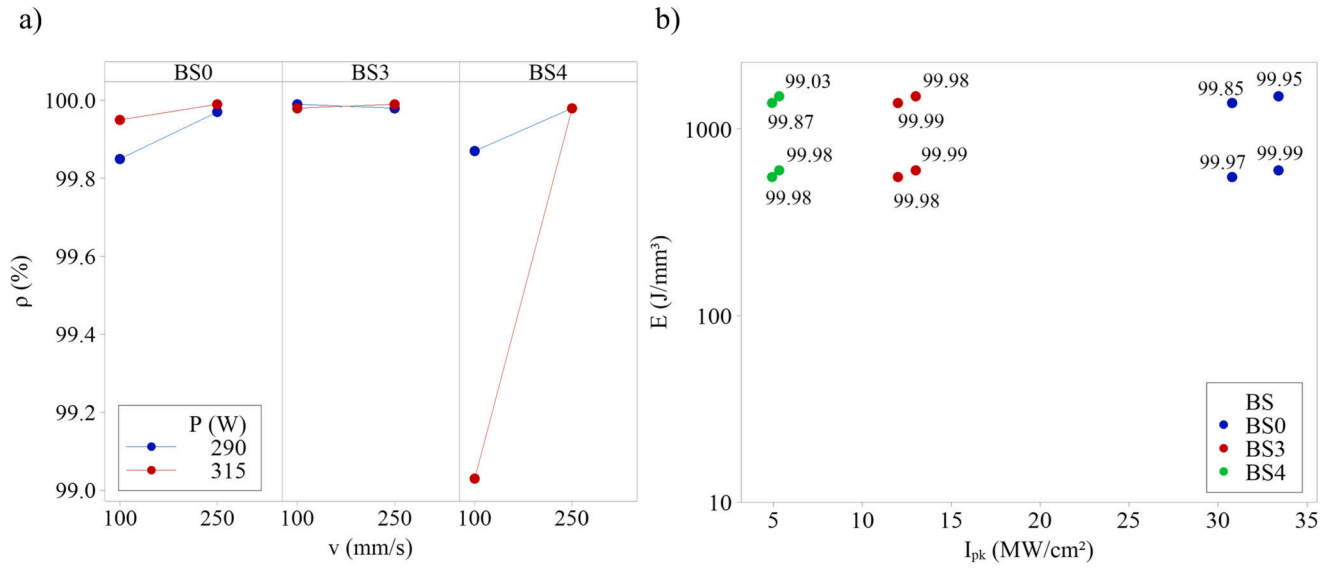

Fig. 11. a) Density (ρ) as a function of process parameters. b) Volumetric energy density (E) vs peak (I_{pk}) intensities for each experimental condition (note that jitter was applied on both axes to data points for readability). Data labels denote the corresponding density.

of the beam profile and the power levels. At $v = 100$ mm/s, the microstructure of the samples produced with indexes BS3-4 features few coarser and larger grains. With index BS0 grains appear to be coarser when reducing speed, but still follow a fibre-like arrangement along the build direction.

Overall, a combination of scan speed and beam shape is required to move the grain structure towards an equiaxed form. At low speed, a microstructure morphology resembling that induced by high temperature annealing is achievable only by using non-Gaussian beam profiles.

3.2.3. Grain size

Fig. 13 shows the *AR* data as a function of beam shape index *BS*, laser power *P* and scan speed *v*. The aim of the validation experiment was to separate the effect of the beam profile from the energy density. Thereby, the effect of beam shape appeared clearly for $v = 100$ mm/s, showing that *AR* could decrease down to 5 only with indexes BS3-4, whereas with BS0 (Gaussian profile) the *AR* is at least doubled. This observation is not valid for $v = 250$ mm/s, where a highly columnar microstructure was found irrespective of the beam shape and power levels.

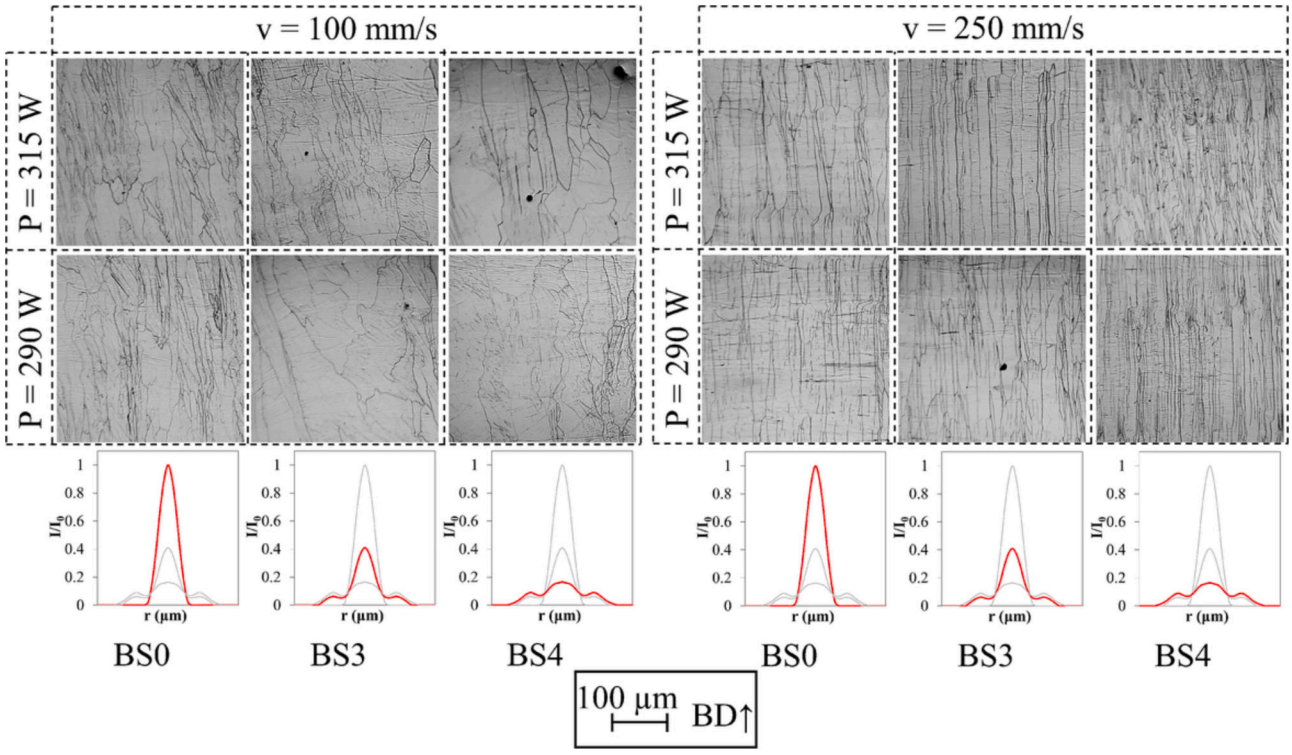

Fig. 12. Microstructure comparison of the process parameter combinations tested in terms of *P*, *v* and beam shape *BS* (BD: Build Direction).

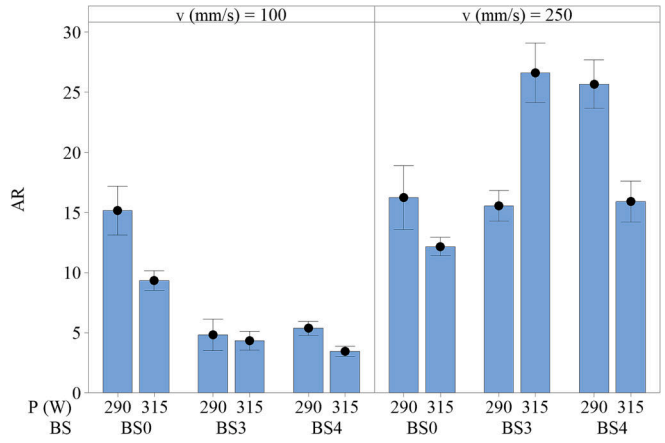

Fig. 13. *AR* as a function of beam shape index (*BS*), laser power (*P*) and scan speed (*v*). Interval bars refer to the standard error.

3.2.4. *Crystallographic texture*

EBSD analysis was conducted to identify the crystallographic texture on four highly dense ($\rho > 99.5$ %) samples produced with all the tested irradiance conditions (I_{pk} and I_r) at the scan speed of 100 mm/s. These conditions were chosen to investigate the sole effect of the beam profile structure on crystallographic texture.

Fig. 14a–d shows the resulting {1 0 0} Pole Figures (PF) for the samples produced with $I_{pk} = I_0/2$, $I_{pk} = I_0$, $I_{pk} = I_0/2 - I_r = 0.2I_0$ and $I_{pk} = I_0 - I_r = 0.2I_0$. To facilitate comprehension of the process parameter combinations, 2D irradiance profiles are shown above each PF. The calculated texture indexes are indicated below each PF as well as the Inverse Pole Figures (IPF) along the Z direction with grain boundaries at a 5° misorientation angle [43].

Under the conditions in which $I_{pk} = I_0/2$, a dominant pole with a (1 0 0) crystalline arrangement is observed, exhibiting a slight misorientation in relation to the normal direction. This phenomenon could be attributed to the convective flow of inert gas utilized during the process. The PF plots shown in Figs. 14a-c are consistent with the morphological orientation of the columnar and elongated grains shown in Fig. 8. Indeed, the elongated grains show a fibre-like arrangement along the build direction, or (1 0 0) direction, that is the easy-growth direction for cubic materials. Similar observations were already presented in the work of Garibaldi et al. [43] dealing with a similar iron silicon composition. Around the main pole, Figs. 14a-c also shows the formation of a ring-like arrangement. The formation of this ring texture is well-known and depends on the 67°-rotational scanning strategy used during processing [44]. However, the use of an I_r made it possible to change the appearance of this ring. Indeed, with $I_r = 0.2I_0$, the outer ring texture is disrupted thus revealing the main outer poles referred to the (1 0 0) direction. From the IPF, the grain structure was also significantly altered. Few large and coarse grains substituted a multitude of elongated grains when I_r was adopted. The texture observed was still a mixture of ⟨1 0 1⟩ and ⟨1 1 1⟩, but the sample produced with $I_{pk} = I_0/2 - I_r = 0.2I_0$ (Fig. 14c) was much more texturized, as demonstrated from the doubled *TI* as well.

Similar observations also apply for the conditions shown in Fig. 14b-d, with $I_{pk} = I_0$. In this case, the sample produced with a Gaussian profile was not texturized, as observed from the PF and its *TI* value. On the other hand, the sample produced with additional I_r showed a much stronger ⟨1 0 0⟩ texture with *TI*.

Additional evidence of grain enlargement induced by ring-shaped profiles came from the grain boundary density calculation. Within the same acquisition field and $I_{pk} = I_0/2$, grain boundary density decreases from 0.5854 1/μm for the Gaussian condition to 0.0966 1/μm with the addition of I_r. With $I_{pk} = I_0$, grain boundary density is reduced from 0.2091 1/μm to 0.1139 1/μm when I_r is applied.

4. Understanding the effect of irradiance profile on grain structure

In general, the results indicate that ring-shaped irradiance profiles enable the modification of both the microstructure and texture of samples produced. Moreover, it was observed that this approach ensured

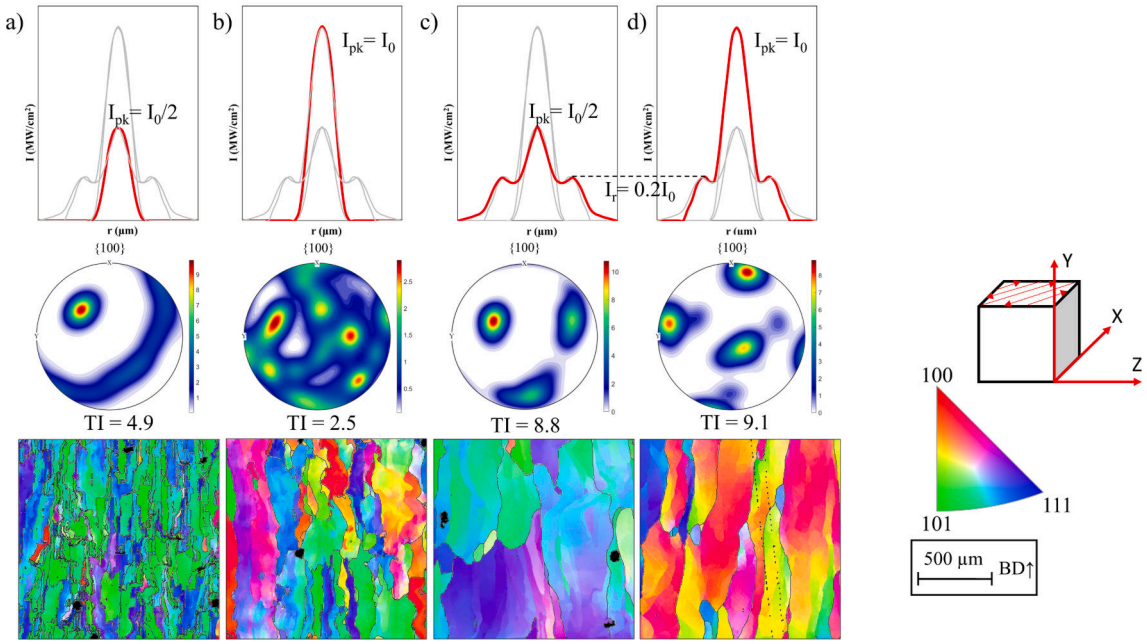

Fig. 14. PF and IPF along Z obtained from as-built samples built with all the tested irradiance conditions (I_{pk}, I_r) and for speed $v = 100$ mm/s. a) $I_{pk} = I_0/2$, $I_r = 0$; b) $I_{pk} = I_0$, $I_r = 0$; c) $I_{pk} = I_0/2$, $I_r = 0.2I_0$; d) $I_{pk} = I_0$, $I_r = 0.2I_0$ (BD: Build Direction). Texture indexes are reported below each PF.

satisfactory densification as shown in Fig. 15a-b. It appeared, without any reasonable doubt, that only with ring shaped profiles (index BS3-4) the grain *AR* could be reduced below 5, as shown in Fig. 15b. Meanwhile, at the same energy density levels (>1000 J/mm^3) samples produced with a Gaussian profile (index BS0) feature grain *AR* of between 9 and 15. Moreover, as illustrated in Fig. 15c, the lack of correlations between *AR* and ρ data suggested that grain size appears to be independent from relative density.

Average grain size estimation procedures performed on large and planar acquisition fields should usually require grain mapping via the EBSD technique and the application of rigorous and reproducible criteria defined by standards, such as the ISO 13067:2020 [45] or the ASTM E2627 [46]. Despite the quantity of data extractable from a single acquisition, EBSD mapping of large experimental campaigns is time-consuming. The procedure for average grain size described was motivated by the necessity of systematically representing the effect of process parameters, particularly those related to irradiance, on the manipulation of microstructure. The results indicate that the grain morphology tends to approach an equiaxed shape, resembling what is observed during the heat treated stage, even though the *AR* values are higher than 2 [42]. The findings from optical microscopy and IPF observations provide confirmation that utilization of ring beam shapes has a dual effect on microstructure. Firstly, it leads to the formation of larger and coarser grains that elongate along the build direction, replacing the conventional fibre-like arrangement. Secondly, it enhances the crystallographic texture. It must be highlighted that volumetric energy density is not necessarily capable of capturing the physics behind the PBF-LB/M process, despite its common usage as measure of the nominal energy released to the material [47]. Diverse values of energy density, or equivalently in terms of power and speed combination, can likely result in different melt pool dynamics. Nonetheless, the objective of this study is not to determine which melting mechanism occurs at a single-track level. Instead, the scope is to demonstrate that other parameters beyond energy density, such as the beam profile, can affect the material properties.

Accordingly, this paper explores the impact of energy density and beam profile, decoded with peak and ring intensities, to evaluate how part quality and material properties change on a macroscale level. Future works employing multi-physics simulations will likely elucidate the main effects and interactions of the various phenomena acting during the process. However, since simulation are commonly performed on single-track conditions, they will hardly resolve the macroscale behaviour of the material owing to the multi-layer nature of the process.

Fig. 16a-d illustrates the development of the melt pool and grain structure using different peak and ring intensities, but at the same scan speed ($v = 100$ mm/s). Note that the curves that represent the melt pool and grain boundaries are only hypothetical since they could not be measured. As depicted, peak and ring intensities have different effects on the melt pool shape. Specifically, the peak intensity mostly regulates the melt pool depth, whereas the ring intensity affects the melt pool width. Therefore, beam profiles with the same peak intensity are expected to produce similar melt pool depths, whereas those with the same ring intensity should generate similar melt pool widths. This is evident when indicatively comparing the melt pool width from frames of Fig. 16a-b with Fig. 16c-d. By regulating the intensity profile in terms of peak and ring intensity, it is possible to manipulate the cooling gradients, which drive the evolution of the grain structure. For example, by combining ring beam profiles with high energy density, the melt pool size can be enlarged, leading to a higher percentage of remelting between consecutive layers and orienting the cooling rate vectors towards the build direction, as illustrated in Fig. 16c-d. This mutual effect promotes the epitaxial growth of grains between two consecutive layers resulting in coarser and larger grains, but still stretched along the build direction, as observed from the *AR* measurements. In contrast, using the Gaussian profile does not offer the same flexibility in terms of melt pool and grain structure manipulation, as depicted in Fig. 16a-b. Indeed, although the peak intensity of the beam profile appears to have a moderate effect on grain size, higher energy density levels combined with a Gaussian distribution are expected to result in a highly columnar and anisotropic microstructure.

5. Discussion

This work demonstrates that the capability of in-source dynamic beam shaping within an PBF-LB/M process offers increased flexibility, allowing for enhanced control of microstructure and texture of the parts

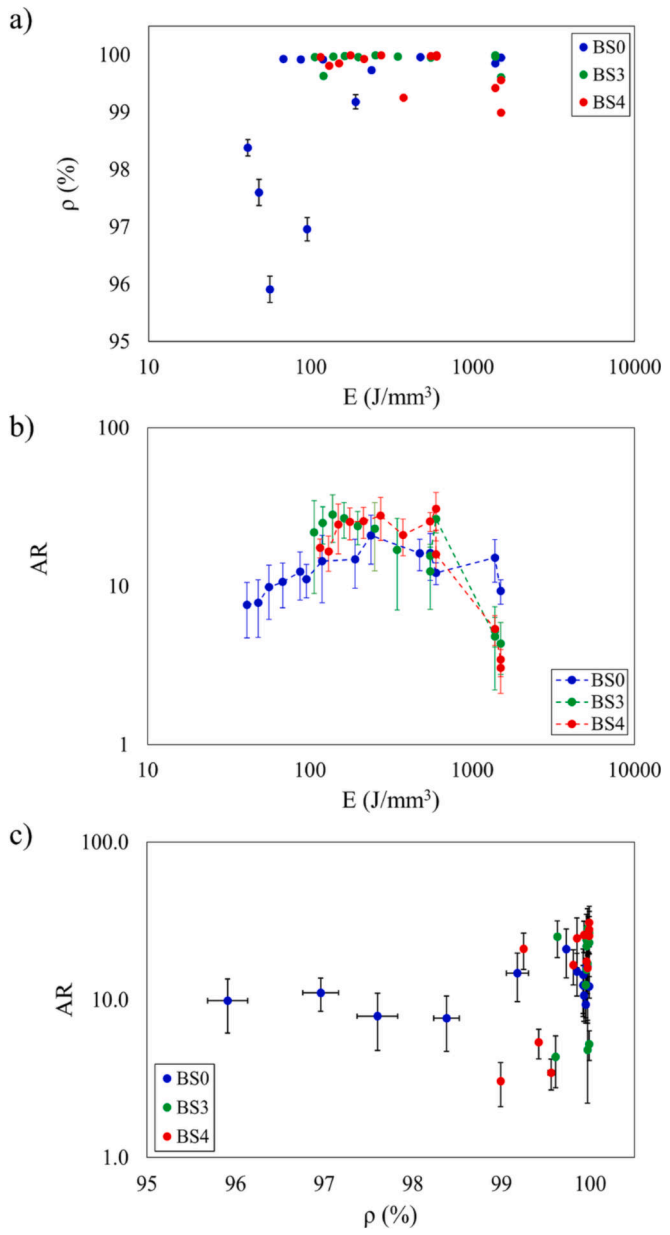

Fig. 15. a) Overall grain aspect ratio (*AR*) and b) relative density (ρ) as a function of volumetric energy density (*E*) for the beam shapes (*BS*) tested. c) Grain aspect ratio as a function of relative density. Interval bars refer to standard deviations while *AR* and *E* scales are displayed in bilogarithmic dimensions. Experimental conditions with $\rho < 95$ % are omitted.

produced. Grain size, orientation and crystallographic texture play a crucial role in the control of functional properties. Hence, the magnetic properties of Si-based alloys are often optimised using special heat treatments aimed at manipulating the microstructure properties [41]. Switching the beam profile on-the-fly to modify the microstructure locally could be a game-changing development for laser sources. Such a solution can be employed to optimise the magnetic properties of Si-based alloys without necessarily having post heat treatments. Given that post-annealing treatments of Si-based electrical steels typically require expensive and specialised furnaces operating with high temperatures (>1100 °C) and controlled atmosphere [48], the utilization of beam shaping emerges as a pathway to avoid such passages.

Numerous other techniques for correcting and preventing defects, including remelting, have been proposed in Laser Powder Bed Fusion (PBF-LB/M) to enhance surface finish and density [49], reduce spatter emission via keyhole stabilisation [50], and particularly to manipulate microstructures by enlarging grains [51]. Applying a remelting strategy with Gaussian beams provided by conventional single-core fibre laser sources may be configured as a solution for tailoring the microstructure at the expense of reduced productivity. However, a Gaussian irradiance distribution reproduces a temperature profile on the workpiece described by a similar Gaussian function [52]. Despite being commonly employed in PBF-LB/M, Gaussian beam profiles are less controllable because power is mostly localised in the centre of the distribution. This inefficient power distribution is sometimes addressed as the cause of local overheating, evaporation and spatter emission [53]. Instead, customised irradiance profiles generated by multi-core fibre lasers can be tuned to tailor the temperature profile experienced by the material, leading to more precise control over the material's microstructure.

Ring beams can be used as an alternative to Gaussian profiles for tailoring the grain structure of materials, allowing for manipulation of the material's properties and offering numerous design possibilities for stator/rotor cores. By adapting the microstructure of the material to the magnetic flux, the path of the magnetic flux can be optimised topologically without any design constraints. For example, an equiaxed grain morphology can be used when maximum magnetic permeability is desirable, while stretched or oriented grain morphologies can be utilised to achieve more directional magnetic properties. Therefore, the spatial beam shaping technique offers greater process flexibility than remelting strategies or post annealing heat treatments, making it a promising approach for the construction of next-generation electric motors, especially when combined with other well-known design strategies, such as structural material grading induced by air/powder gaps.

6. Conclusions

In this work, a soft magnetic Fe-2.9wt.%Si alloy is processed using a multi-core fibre laser source with in-source beam shaping capabilities to produce small prismatic samples via PBF-LB/M. The results confirmed the direct impact of irradiance properties of the laser beam on the microstructural properties of the alloy processed. The overall results can be summarised as follows:

- Two shape encoding parameters, peak (I_{pk}) and ring (I_r) intensities, were introduced to decode the structure of the beam profiles. Accordingly, an experimental study based on an irradiance parametric scheme was designed to evaluate the effect of ring-shaped distribution on density and microstructural properties.
- Adequate densification can be achieved with Fe-Si2.9 wt% alloy independently from the beam shape. The main driving factor is the energy density. As with common PBF-LB/M alloys, lack-of-fusion and keyhole pores occur as a function of variation of the energy density.
- In the lower end of the energy density conditions tested, the microstructure of Fe-Si2.9 wt% was columnar with grains elongated along the build direction. This microstructure is common to PBF-LB/M processed Fe-Si alloys, which is often homogenised by means of dedicated heat treatments.
- Additional ring intensity (I_r) provided modification of the grain morphology, reducing the aspect ratio (*AR*) towards less marked columnar structures in the lower end of the energy density values.
- In order to move towards equiaxed grains both high energy density ($E > 1000$ J/mm^3) and ring shaped beams are required.
- The results showed that grain size enlargement induced by ring-shaped distributions is accompanied by intrinsic higher texturization.

The results of this work provided initial quantitative indications on how novel in-source beam shaping capabilities can add flexibility to PBF-LB/M. The work demonstrated that manipulation of the irradiance profile enables a wider margin of microstructural property control

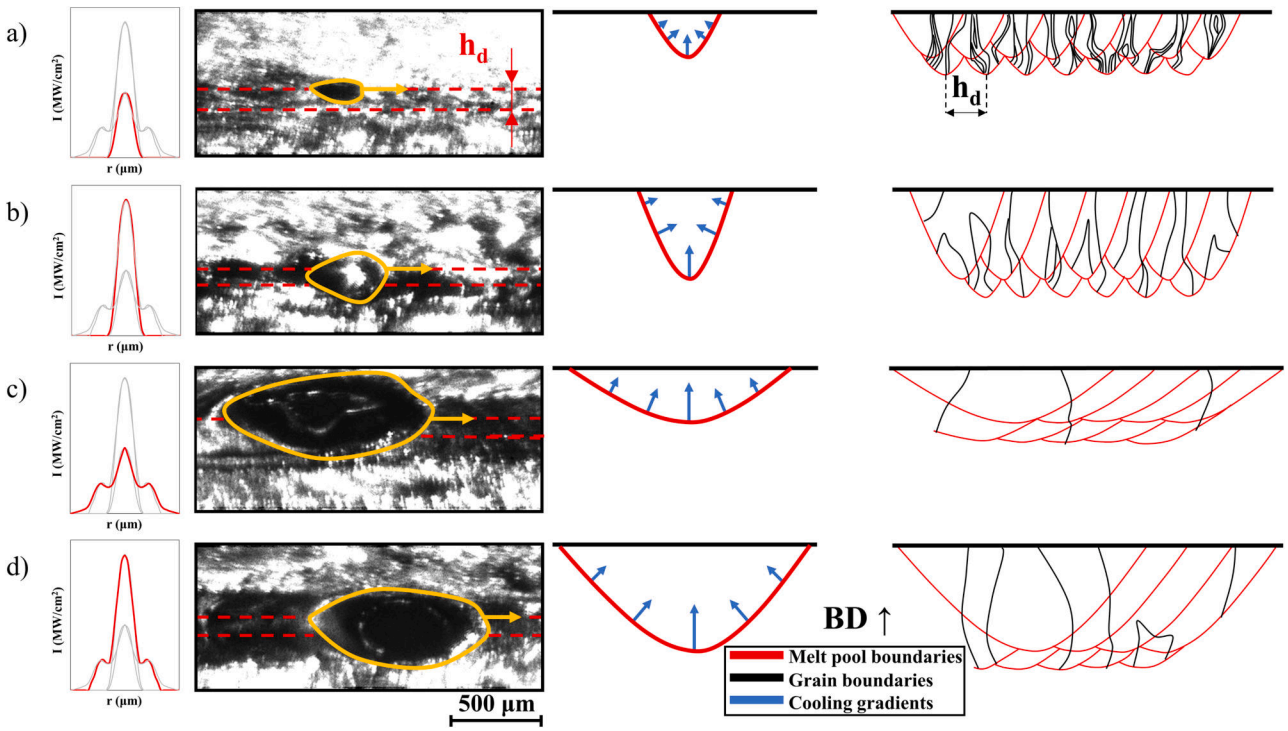

Fig. 16. Representative frames of the melt pool acquired via high-speed imaging, schematisation of the melt pool and grain structure evolution for the conditions tested with a) I_{pk} = 5.3 MW/cm^2/ I_r = 0 MW/cm^2, b) I_{pk} = 10.6 MW/cm^2/ I_r = 0 MW/cm^2, c) I_{pk} = 5.3 MW/cm^2/ I_r = 2.1 MW/cm^2 and d) I_{pk} = 10.6 MW/cm^2/ I_r = 2.1 MW/cm^2. The curves representing melt pool and grain boundaries are only indicative. (BD: Build Direction).

which can be extremely advantageous for the design of new electromagnetic core concepts made of soft magnetic alloys. Engineering the microstructure of as-built parts via spatial beam shaping means having control over the functional properties already achievable during the process. However, to consider beam shaping as a reproducible tool, a more rigorous description of the beam characteristics should be accomplished. In this work, two irradiance-based parameters were introduced to decode the beam shape. Further attention should be paid to modelling irradiance profiles and the introduction of new shape-encoding parameters which consider the spatial dependence of beam power. In this perspective, beam profile modelling can be further combined with multi-physics simulation or finite element approaches and these results can provide a useful mean for model calibration and validation.

CRediT authorship contribution statement

Francesco Galbusera: Conceptualization, Formal analysis, Investigation, Data curation, Software, Writing – original draft, Writing – review & editing. **Leonardo Caprio:** Methodology, Writing – original draft, Writing – review & editing. **Barbara Previtali:** Methodology, Supervision, Resources, Writing – original draft, Writing – review & editing. **Ali Gökhan Demir:** Conceptualization, Methodology, Supervision, Formal analysis, Investigation, Writing – original draft, Writing – review & editing.

Declaration of competing interest

The authors declare that they have no known competing financial interests or personal relationships that could have appeared to influence the work reported in this paper.

Data availability

Data will be made available on request.

Acknowledgements

The authors acknowledge the support of the Italian Ministry of University and Education (MIUR, Italy) through the National Recovery and Resilience Plan (PNRR). The authors are thankful to nLIGHT Inc. (United States) and Optoprim Srl (Italy) for the laser source used throughout the experimental activity. The authors would like to thank BLM Group (Italy) for providing the high-speed imaging camera and illumination light. Raylase GmbH (Germany) and Direct Machining Control (Lituania) are acknowledged for the technical support and the continuous development of the products used during the project. In addition, the authors thank Ömer Alperen Çalışkan for his help with fabrication and investigation of the samples presented in this work.

References

[1] H. Tiismus, A. Kallaste, T. Vaimann, A. Rassõlkin, State of the art of additively manufactured electromagnetic materials for topology optimized electrical machines, Additive Manufacturing 55 (2022), https://doi.org/10.1016/j.addma.2022.102778. Elsevier B.V.
[2] B. Koo, et al., Structurally-layered soft magnetic Fe-Si components with surface insulation prepared by shell-shaping selective laser melting, Appl Surf Sci 553 (Jul. 2021), https://doi.org/10.1016/j.apsusc.2021.149510.
[3] A. Selema, M.N. Ibrahim, P. Sergeant, Metal Additive Manufacturing for Electrical Machines Technology Review and Latest Advancements, Energies 15 (3. MDPI) (2022), https://doi.org/10.3390/en15031076.
[4] L. Szabó, D. Fodor, The Key Role of 3D Printing Technologies in the Further Development of Electrical Machines, Machines 10 (5. MDPI) (2022), https://doi.org/10.3390/machines10050330.
[5] M.U. Naseer, A. Kallaste, B. Asad, T. Vaimann, A. Rassõlkin, A review on additive manufacturing possibilities for electrical machines, Energies 14 (7. MDPI AG) (2021), https://doi.org/10.3390/en14071940.
[6] S. Gao, et al., Effect of Laser Energy Density on Surface Morphology, Microstructure, and Magnetic Properties of Selective Laser Melted Fe-3wt.% Si Alloys, J Mater Eng Perform 30 (7) (Jul. 2021) 5020–5030, https://doi.org/10.1007/s11665-021-05591-w.
[7] T.N. Lamichhane, L. Sethuraman, A. Dalagan, H. Wang, J. Keller, M. P. Paranthaman, Additive manufacturing of soft magnets for electrical machines—a review, Materials Today Physics 15 (2020) 100255, https://doi.org/10.1016/j.mtphys.2020.100255.

[8] H. Tiismus, et al., Ac magnetic loss reduction of slm processed fe-si for additive manufacturing of electrical machines, Energies (basel) 14 (5) (Mar. 2021), https://doi.org/10.3390/en14051241.

[9] J. Yang, Z. Fu, C. Körner, Structure Design of Soft Magnetic Materials using Electron Beam-based Additive Manufacturing, Adv. Mater. (Apr. 2023), https://doi.org/10.1002/adma.202300837.

[10] H. Tiismus, A. Kallaste, M.U. Naseer, T. Vaimann, A. Rassolkin, Design and Performance of Laser Additively Manufactured Core Induction Motor, IEEE Access 10 (2022) 50137–50152, https://doi.org/10.1109/ACCESS.2022.3173317.

[11] A. Plotkowski, et al., Influence of scan pattern and geometry on the microstructure and soft-magnetic performance of additively manufactured Fe-Si, Addit Manuf 29 (Oct. 2019), https://doi.org/10.1016/j.addma.2019.100781.

[12] D. Goll, et al., Additive manufacturing of soft magnetic materials and components, Addit Manuf 27 (May 2019) 428–439, https://doi.org/10.1016/j.addma.2019.02.021.

[13] N. Urban, L. Bauch, R. Armbruster, J. Franke, Evaluation of soft magnetic ferrosilicon FeSi 6.5 for laser beam melting, in: *2019 9th International Electric Drives Production Conference, EDPC 2019 - Proceedings*, pp. 2019–2022, 2019, doi: 10.1109/EDPC48408.2019.9011973.

[14] M. Garibaldi, I. Ashcroft, J.N. Lemke, M. Simonelli, R. Hague, Effect of annealing on the microstructure and magnetic properties of soft magnetic Fe-Si produced via laser additive manufacturing, Scr Mater 142 (2018) 121–125, https://doi.org/10.1016/j.scriptamat.2017.08.042.

[15] S. Urbanek, et al., Design and Experimental Investigation of an Additively Manufactured PMSM Rotor, in: In *2021 IEEE International Electric Machines and Drives Conference, IEMDC 2021*, Institute of Electrical and Electronics Engineers Inc., May 2021, https://doi.org/10.1109/IEMDC47953.2021.9449566.

[16] M. Garibaldi, C. Gerada, I. Ashcroft, R. Hague, Free-Form Design of Electrical Machine Rotor Cores for Production Using Additive Manufacturing, J. Mech. Des., Trans. ASME 141 (7) (Jul. 2019), https://doi.org/10.1115/1.4042621.

[17] L. Gargalis, et al., Additive manufacturing and testing of a soft magnetic rotor for a switched reluctance motor, IEEE Access 8 (2020) 206982–206991, https://doi.org/10.1109/ACCESS.2020.3037190.

[18] H. Tiismus, A. Kallaste, A. Belahcen, A. Rassölkin, T. Vaimann, P.S. Ghahfarokhi, Additive manufacturing and performance of E-Type transformer core, Energies (basel) 14 (11) (Jun. 2021), https://doi.org/10.3390/en14113278.

[19] A. Plotkowski, et al., Design and performance of an additively manufactured high-Si transformer core, Mater Des 194 (Sep. 2020), https://doi.org/10.1016/j.matdes.2020.108894.

[20] R. Wrobel, B. Mecrow, A Comprehensive Review of Additive Manufacturing in Construction of Electrical Machines, IEEE Trans. Energy Convers. 35 (2) (2020) 1054–1064, https://doi.org/10.1109/TEC.2020.2964942.

[21] G. Stornelli, et al., Properties of additively manufactured electric steel powder cores with increased si content, Materials 14 (6) (Mar. 2021), https://doi.org/10.3390/ma14061489.

[22] J. Grünewald, F. Gehringer, M. Schmöller, K. Wudy, Influence of ring-shaped beam profiles on process stability and productivity in laser-based powder bed fusion of AISI 316L, Metals (basel) 11 (12) (Dec. 2021), https://doi.org/10.3390/met11121989.

[23] J. Grünewald, J. Reimann, K. Wudy, Influence of ring-shaped beam profiles on spatter characteristics in laser-based powder bed fusion of metals, J Laser Appl 35 (4) (Nov. 2023), https://doi.org/10.2351/7.0001153.

[24] T.M. Wischeropp, H. Tarhini, C. Emmelmann, Influence of laser beam profile on the selective laser melting process of AlSi10Mg, J Laser Appl 32 (2) (2020) 022059, https://doi.org/10.2351/7.0000100.

[25] F. Galbusera, L. Caprio, B. Previtali, A.G. Demir, The influence of novel beam shapes on melt pool shape and mechanical properties of LPBF produced Al-alloy, J Manuf Process 85 (Jan. 2023) 1024–1036, https://doi.org/10.1016/j.jmapro.2022.12.007.

[26] F. Nahr, D. Bartels, R. Rothfelder, M. Schmidt, Influence of Novel Beam Shapes on Laser-Based Processing of High-Strength Aluminium Alloys on the Basis of EN AW-5083 Single Weld Tracks, J. Manuf. Mater. Process. 7 (3) (May 2023) 93, https://doi.org/10.3390/jmmp7030093.

[27] M.S. Mohebbi, V. Ploshikhin, Development of fully equiaxed microstructure in Scalmalloy® through powder bed fusion using a ring-mode laser beam, Scr Mater 236 (Nov. 2023), https://doi.org/10.1016/j.scriptamat.2023.115680.

[28] T.T. Roehling, et al., Controlling grain nucleation and morphology by laser beam shaping in metal additive manufacturing, Mater Des 195 (2020) 109071, https://doi.org/10.1016/j.matdes.2020.109071.

[29] R. Shi, S.A. Khairallah, T.T. Roehling, T.W. Heo, J.T. McKeown, M.J. Matthews, Microstructural control in metal laser powder bed fusion additive manufacturing using laser beam shaping strategy, Acta Mater 184 (2020) 284–305, https://doi.org/10.1016/j.actamat.2019.11.053.

[30] M. Cloots, P.J. Uggowitzer, K. Wegener, Investigations on the microstructure and crack formation of IN738LC samples processed by selective laser melting using Gaussian and doughnut profiles, Mater Des 89 (2016) 770–784, https://doi.org/10.1016/j.matdes.2015.10.027.

[31] T.U. Tumkur, et al., Nondiffractive beam shaping for enhanced optothermal control in metal additive manufacturing, Sci Adv 7 (38) (2021) 1–12, https://doi.org/10.1126/sciadv.abg9358.

[32] I.V. Zhirnov, P.A. Podrabinnik, A.A. Okunkova, A.V. Gusarov, Laser beam profiling: Experimental study of its influence on single-track formation by selective laser melting, Mech. Industry 16 (7) (2015), https://doi.org/10.1051/meca/2015082.

[33] A. Metel, M. Stebulyanin, S. Fedorov, A. Okunkova, Power Density Distribution for Laser Additive Manufacturing (SLM): Potential, Fundamentals and Advanced Applications, Technologies (basel) 7 (1) (2018) 5, https://doi.org/10.3390/technologies7010005.

[34] L. Caprio, A. G. Demir, B. Previtali, Observing molten pool surface oscillations during keyhole processing in laser powder bed fusion as a novel method to estimate the penetration depth, *Addit Manuf*, no. July 2020 (2020) 101470, doi: 10.1016/j.addma.2020.101470.

[35] L. Mazzoleni, L. Caprio, M. Pacher, A.G. Demir, External Illumination Strategies for Melt Pool Geometry Monitoring in SLM, JOM (2018), https://doi.org/10.1007/s11837-018-3209-1.

[36] K. Schricker *et al.*, Characterization of keyhole dynamics in laser welding of copper by means of high-speed synchrotron X-ray imaging, in: *Procedia CIRP*, Elsevier B. V., 2022, pp. 501–506. doi: 10.1016/j.procir.2022.08.079.

[37] nLIGHT Inc, AFX User Manual Single-mode Fiber Laser with Programmable Beam Shaping, 2020.

[38] W.M. Steen, J. Mazumder, in: Laser material processing, Springer, London, 2010, https://doi.org/10.1007/978-1-84996-062-5.

[39] S. D'Arcangelo, et al., Comprehensive benchmarking of laser welding technologies including novel beam shapes and wavelengths for e-drive copper hairpins, Opt Laser Technol 169 (Feb. 2024), https://doi.org/10.1016/j.optlastec.2023.109964.

[40] F. Galbusera, A. G. Demir, J. Platl, C. Turk, R. Schnitzer, B. Previtali, Processability and cracking behaviour of novel high-alloyed tool steels processed by Laser Powder Bed Fusion, *J Mater Process Technol*, no. August, 2021, doi: 10.1016/j.jmatprotec.2021.117435.

[41] M. Garibaldi, I. Ashcroft, N. Hillier, S.A.C. Harmon, R. Hague, Relationship between laser energy input, microstructures and magnetic properties of selective laser melted Fe-6.9%wt Si soft magnets, Mater Charact 143 (November 2017) (2018) 144–151, https://doi.org/10.1016/j.matchar.2018.01.016.

[42] V.B. Biscuola, M.A. Martorano, Mechanical blocking mechanism for the columnar to equiaxed transition, Metall Mater Trans A Phys Metall Mater Sci 39 (12) (2008) 2885–2895, https://doi.org/10.1007/s11661-008-9643-x.

[43] M. Garibaldi, I. Ashcroft, M. Simonelli, R. Hague, Metallurgy of high-silicon steel parts produced using Selective Laser Melting, Acta Mater 110 (2016) 207–216, https://doi.org/10.1016/j.actamat.2016.03.037.

[44] J.D. Pérez-Ruiz, L.N.L. de Lacalle, G. Urbikain, O. Pereira, S. Martínez, J. Bris, On the relationship between cutting forces and anisotropy features in the milling of LPBF Inconel 718 for near net shape parts, Int J Mach Tools Manuf 170 (Nov. 2021), https://doi.org/10.1016/j.ijmachtools.2021.103801.

[45] C. Chang *et al.*, Achieving ultra-high strength and ductility in Mg–9Al–1Zn–0.5Mn alloy via selective laser melting, *Adv. Powder Mater.* 2(2) (2023) 100097, doi: 10.1016/j.apmate.2022.100097.

[46] R. Savinov, Y. Wang, J. Wang, J. Shi, Comparison of microstructure and properties of CoCrFeMnNi high-entropy alloy from selective laser melting and directed energy deposition processes, in: *Procedia Manufacturing*, Elsevier B.V., 2021, pp. 435–442. doi: 10.1016/j.promfg.2021.06.046.

[47] U. Scipioni Bertoli, A. J. Wolfer, M. J. Matthews, J. P. R. Delplanque, J. M. Schoenung, On the limitations of Volumetric Energy Density as a design parameter for Selective Laser Melting, *Mater Des* 113 (2017) 331–340, doi: 10.1016/j.matdes.2016.10.037.

[48] M. Quercio, et al., Functional characterization of L-PBF produced FeSi2.9 Soft Magnetic Material, in: In *2022 International Conference on Electrical Machines, ICEM 2022*, 2022, https://doi.org/10.1109/ICEM51905.2022.9910684.

[49] A.G. Demir, B. Previtali, Investigation of remelting and preheating in SLM of 18Ni300 maraging steel as corrective and preventive measures for porosity reduction, Int. J. Adv. Manuf. Technol. 93 (5–8) (Nov. 2017) 2697–2709, https://doi.org/10.1007/s00170-017-0697-z.

[50] D. Xie, F. Lv, L. Shen, Z. Tian, R. Jiang, J. Zhao, Effect of higher laser power remelting on porosity and mechanical performance of part built by laser powder bed fusion, Int. J. Adv. Manuf. Technol. (Feb. 2023), https://doi.org/10.1007/s00170-023-11067-z.

[51] M.S. Moyle, N. Haghdadi, X.Z. Liao, S.P. Ringer, S. Primig, On the microstructure and texture evolution in 17–4 PH stainless steel during laser powder bed fusion: Towards textural design, J Mater Sci Technol 117 (Aug. 2022) 183–195, https://doi.org/10.1016/j.jmst.2021.12.015.

[52] A. Laskin, J. Volpp, V. Laskin, T. Nara, S.R. Jung, Multispot optics for beam shaping of high-power single-mode and multimode lasers, J Laser Appl 33 (4) (2021) 042046, https://doi.org/10.2351/7.0000461.

[53] S. N. Grigoriev *et al.*, Beam Shaping in Laser Powder Bed Fusion: Péclet Number and Dynamic Simulation, *Metals (Basel)* 12(5) (2022), doi: 10.3390/met12050722.